


# Evaluation of the capacity surfaces of reinforced concrete sections: Eurocode versus a plasticity-based approach

Salvatore Sessa  · Francesco Marmo · Luciano Rosati · Leonardo Leonetti · Giovanni Garcea · Raffaele Casciaro

Received: 12 April 2017 / Accepted: 7 November 2017  
© Springer Science+Business Media B.V., part of Springer Nature 2017

**Abstract** The classical Eurocode-compliant ultimate limit state (ULS) analysis of reinforced concrete sections is investigated in the paper with the aim of verifying if and how this well-established design procedure can be related to plasticity theory. For this reason, a comparative analysis concerning capacity surfaces of reinforced concrete cross sections, computed via a ULS procedure and a limit analysis approach, is presented. To this end, a preliminary qualitative discussion outlines modeling assumptions aiming to reproduce the physical behavior of reinforced concrete cross sections with respect to ductility

and confinement issues. Besides the theoretical importance of the proposed approach, numerical experiments prove that limit analysis yields not only very accurate results but also a computationally effective procedure that can be affordably used in common design practice.

**Keywords** Ultimate limit state · Reinforced concrete · Limit analysis · Capacity surface

## 1 Introduction

Still nowadays safety checks of reinforced concrete (r.c.) sections, especially when subjected to seismic loads, is a challenging problem [6, 7]. Actually a complex behavior due to geometry, constitutive nonlinearities and external loads has to be accounted for in computational methods.

In the case of reinforced concrete framed structures, provisions of several standard codes, including Eurocode 2 [9], define ultimate limit states (ULS) associated with flexural behavior in terms of maximum strain values for each material used in the structural models. In particular, safety checks are performed by capacity domains which characterize the attainment of the ULS by internal forces defined as a combination of the axial force and two bending moments.

In spite of their widespread use in structural analysis, it is quite surprising to record that the

---

S. Sessa (✉) · F. Marmo · L. Rosati  
Department of Structures for Engineering and  
Architecture, University of Naples Federico II, Naples,  
Italy  
e-mail: salvatore.sessa2@unina.it

F. Marmo  
e-mail: f.marmo@unina.it

L. Rosati  
e-mail: rosati@unina.it

L. Leonetti · G. Garcea · R. Casciaro  
Dipartimento di Ingegneria Informatica, Modellistica,  
Elettronica e Sistemistica, Università della Calabria,  
Rende, CS, Italy  
e-mail: leonardo.leonetti@unical.it

G. Garcea  
e-mail: giovanni.garcea@unical.it

R. Casciaro  
e-mail: raffaele.casciaro@unical.it

mechanical context in which the safety checks are actually carried out is substantially unknown or, at least, unspecified. For instance, one does not even know if the nonlinear analysis typically required by ULS checks has to be considered as a nonlinear elastic analysis or a plastic one; nor the above mentioned theoretical drawbacks are somehow compensated by a simple numerical procedure since calculation of the points belonging to the ULS surface usually requires iterative procedures performing computationally demanding operations [24, 25].

Moreover, recently developed analysis typologies, involving several load combinations [18] or seismic envelopes [30, 31, 35], require a great amount of capacity checks; thus, their use in common practice is hampered by the great computational effort of determining a large set of points belonging to the ULS surface.

Thus, one naturally wonders if an alternative approach, grounded on a firm mechanical basis, can actually be exploited. In this respect, the natural candidate is represented by limit analysis [20, 32] and shakedown [40], and related static [27] and kinematic [16] theorems, since it is capable to overcome drawbacks affecting traditional procedures.

In particular, it allows one to evaluate limit values of loads and material strength, neglecting transitory loading phases, constitutive relationships and self-equilibrated stress states [4].

With specific reference to reinforced concrete structures, limit analysis is an affordable and reliable procedure since their design is often based on simplified and conventional procedures [13] aiming to characterize the structural model by catching the essential aspects of its behavior and overcoming the limited knowledge of the constitutive model [5]. An excessive care for detailed modeling of the structural behavior is often in contrast with lack of information available to the designers so that accuracy improvements, with respect to more concise and essential strategies, can only be illusory.

Obviously, in order to correctly apply limit analysis to r.c. sections, it is fundamental that Drucker assumption on infinite ductility of the material is ensured. In particular, ductility of structural members should be sufficient to ensure stress redistribution so that the collapse mechanism evaluated by limit analysis can actually take place.

As a matter of fact, in the case of reinforced concrete, several standard codes, including Eurocodes [9], prescribe to properly design stirrups in order to ensure sufficient ductility as a consequence of the confinement effect. Due to its importance, this topic has been extensively investigated over years [2, 12, 14, 34].

Granted for this, a brilliant procedure for computing limit surfaces of r.c. sections has been formulated in [21]. Originally oriented to finite-element shakedown analysis of 3D framed structures [4], the procedure has been recently enhanced in order to account for Eurocode 8—compliant [10] load combinations [18]. The algorithm reduces the computational effort of the limit analysis by lowering redundant constraints [36, 37], without affecting accuracy of the results, and defining the capacity surface by means of a Minkowski sum of ellipsoids.

This is an effective mathematical tool [3] which computes points belonging to multi-dimensional surfaces as function of their gradient. When applied to axial force—biaxial bending capacity checks, the procedure turns out to be computationally more efficient than the majority of classical algorithms.

Extending the approach based on the use of Minkowski sums to ULS capacity check is somehow compromised by the fact that a few *support functions* [3] have to be calibrated on a set of points belonging to the ULS surface. Although viable, at least in line of principle, such a calibration becomes difficult if the values of the gradient to the ULS surface, computed at each calibration point, are unknown; moreover, their evaluation by using finite differences would compromise the efficiency of the whole procedure.

On the contrary, when used to approximate limit surfaces under the assumption of infinite ductility [18, 21], the calibration of support functions becomes straightforward since the surface gradient is known in closed form.

Based on the considerations detailed above, this research aims to investigate at which conditions ULS surfaces can be safely replaced by capacity domains obtained in the hypothesis of infinite ductility.

This represents a quite original and innovative approach with respect to the current state-of-the-art on the subject [24–26, 35, 38] since, besides establishing a firm theoretical basis for the ULS analysis of sections, sets the stage for a computationally viable

and numerically accurate merging of capacity surface evaluation with limit and shakedown [4, 18, 21] analyses of 2D [17] and 3D [1] mixed models aiming to reliability [28] and nonlinear random vibration analysis of structures [8].

To this end, Sect. 2 introduces capacity surfaces for both the ULS and limit analysis. In particular, ULS domains, defined in terms of axial force and biaxial bending, are computed by a fiber-free procedure [24]. Such an unconditionally convergent algorithm, already extended to several typologies of nonlinear analyses [25] and steel/aluminum sections [26], has been chosen because of its capability of computing the exact values of the internal force vector for which ultimate limit states of reinforced concrete polygonal cross sections are attained.

Ductility of concrete is addressed in Sect. 3 where a Mander [22, 23] constitutive relationship is introduced. In particular, the behavior of a rectangular cross section subject to both uniaxial and biaxial bending is analyzed in order to investigate the influence of confinement and softening on the ultimate limit states. Moreover, peculiar focus is dedicated to the presence of non-confined concrete covers where the first attainment of the compressive ultimate limit state usually occurs.

Considerations reported in Sect. 3 support the definition of a conventional procedure for approximating the capacity surface by elastic domains computed by means of limit analysis based on infinite ductility of concrete. A comparison between elastic domains and ULS surfaces computed for two cross sections is reported in Sect. 4 both in terms of internal forces and collapse mechanisms. Numerical results prove that such an approximation, oriented to safety checks, turns out to be reasonably accurate even with confinement ratios ordinarily assumed in common practice structural design.

Closure reported in Sect. 5 discusses the limitation of the proposed strategy and outlines future research directions aiming to a wider use of the analyzed tools in nonlinear structural analysis.

## 2 Capacity of reinforced concrete sections

Following the provisions of most of the national building codes, evaluation of axial force—biaxial bending capacity of reinforced concrete sections is

usually performed by means of conventional procedures which assume both steel reinforcements and concrete to present uniaxial behavior. This assumption implicitly entails that flexural behavior of the frame element that includes the section is not coupled with shear and torque so that capacity checks with respect to those latter loads can be neglected or computed separately.

Moreover, Eurocode 8 [10] provisions prescribe the employment of an elastic—perfectly plastic constitutive law for steel reinforcement bars and a tensile-only parabola—rectangle stress—strain relationship for concrete. Although very popular, such relationships are approximated, therefore, several alternatives have been developed on years [2, 12, 14, 22, 23, 34].

Regardless of the peculiar constitutive relationships assigned to the employed materials, the mechanical properties of frames are modeled by means of composite cross-sections  $\Omega$  defined as polygonal concrete regions reinforced by clustered steel bars, as shown in Fig. 1.

Assuming a local reference system where axis  $x_1$  is directed along the frame length and axes  $x_2$  and  $x_3$  lay on the cross-section plane, the non-zero stress component is addressed as  $\sigma_{11}$ . Moreover, each polygonal region is defined by means of the coordinates of its  $n_c$  vertexes  $\mathbf{x}_{c,j} = \{x_{2c,j}, x_{3c,j}\}$  while  $n_r$  steel reinforcements are characterized by their area  $A_j$  and location  $\mathbf{x}_j = \{x_{2j}, x_{3j}\}, j = 1, \dots, n_r$ .

Assuming that strain component  $\epsilon_{11}(x_2, x_3)$  are linearly distributed over  $\Omega$ , it is possible to define the generalized strain vector as:

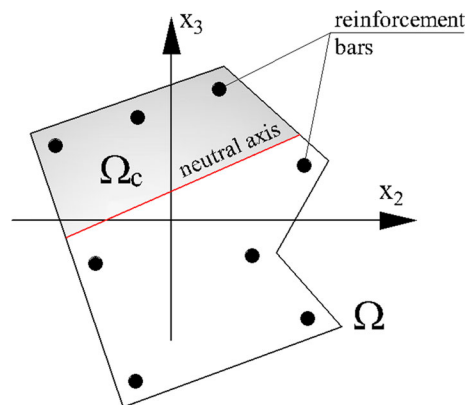


Fig. 1 Typical RC cross section

$$\boldsymbol{\varepsilon} = [\varepsilon_0 \quad \chi_2 \quad \chi_3]^T \tag{1}$$

where  $\varepsilon_0$  is the value of strain component  $\varepsilon_{11}$  at the geometrical center of the cross section and  $\chi_2$  and  $\chi_3$  are the components of the cross-section curvature around axes  $x_2$  and  $x_3$ , respectively. The strain field is therefore defined by linear combination of the generalized strain:

$$\varepsilon_{11}(\boldsymbol{\varepsilon}, \bar{\mathbf{x}}) = \varepsilon_0 + \chi_2 x_3 - \chi_3 x_2 = \boldsymbol{\varepsilon}^T \bar{\mathbf{x}} \tag{2}$$

where  $\bar{\mathbf{x}} = [1, x_3, -x_2]^T$  includes the coordinates of a generic point of the cross-section.

Stress component  $\sigma_{11}$  is computed by a uniaxial, non-linear constitutive law whose features will be discussed below. Nevertheless, it is worth being emphasized that stress-strain relationships can present either perfect-plasticity, hardening or softening behaviors.

Resultants of the acting stresses are collected in a vector  $\mathbf{t}(\boldsymbol{\varepsilon})$  defined as:

$$\mathbf{t}(\boldsymbol{\varepsilon}) = \begin{bmatrix} N_1 \\ M_2 \\ M_3 \end{bmatrix} = \begin{bmatrix} \int_{\Omega} \sigma_{11} d\Omega \\ \int_{\Omega} +x_3 \sigma_{11} d\Omega \\ \int_{\Omega} -x_2 \sigma_{11} d\Omega \end{bmatrix} \tag{3}$$

Stress integrals can be splitted in order to take account of the concrete polygonal region and of the reinforcing bars separately. In such a case, denoting with  $\sigma_c[\varepsilon_{11}(\boldsymbol{\varepsilon}, \bar{\mathbf{x}})]$  and  $\sigma_s[\varepsilon_{11}(\boldsymbol{\varepsilon}, \bar{\mathbf{x}})]$ , respectively, the uniaxial stress of concrete and steel as a function of the strain, the section resultants can be expressed in a compact form as

$$\mathbf{t}(\boldsymbol{\varepsilon}, \bar{\mathbf{x}}) = \sum_{j=1}^{n_r} \sigma_s[\varepsilon_{11}(\boldsymbol{\varepsilon}, \bar{\mathbf{x}}_j)] \bar{\mathbf{x}}_j \Omega_j + \int_{\Omega_c} \sigma_c[\varepsilon_{11}(\boldsymbol{\varepsilon}, \bar{\mathbf{x}})] \bar{\mathbf{x}} d\Omega \tag{4}$$

where  $\Omega_c$ , represents the concrete compressed region; it is initially unknown since it depends on  $\boldsymbol{\varepsilon}$ .

Supposing that limit values have been enforced to  $\varepsilon_{11}$ , and hence to  $\boldsymbol{\varepsilon}$  according to (2), the associated stress resultants belong to the so-called capacity domain  $\mathbb{T}(\boldsymbol{\varepsilon})$ :

$$\mathbb{T}(\boldsymbol{\varepsilon}) = \{\mathbf{t}(\boldsymbol{\varepsilon}) : \Phi[\mathbf{t}(\boldsymbol{\varepsilon})] \leq 0\}. \tag{5}$$

where  $\Phi[\mathbf{t}(\boldsymbol{\varepsilon})]$  is a yield function depending on geometry and constitutive parameters of the section. In

particular,  $\Phi[\mathbf{t}(\boldsymbol{\varepsilon})]$  is greater than 0 if the stress state  $\mathbf{t}(\boldsymbol{\varepsilon})$  is not compatible with the capacity of the section.

For this reason, in a three-dimensional space, the boundary  $\partial\mathbb{T}(\boldsymbol{\varepsilon})$  of the domain  $\mathbb{T}(\boldsymbol{\varepsilon})$ , defined by the condition  $\Phi[\mathbf{t}(\boldsymbol{\varepsilon})] = 0$ , will be denoted as *capacity surface*.

It is worth being emphasized that shape and amplitude of the stress domain depend on the nonlinear stress-strain relationship, in presence of hardening or softening behaviors, and are strongly related to the limit values of  $\varepsilon_{11}$  strain for concrete and steel.

In order to investigate the chance of applying limit-analysis tools in analyzing reinforced concrete sections, the following subsections specialize the computation of the capacity surfaces in two typologies:

1. *Ultimate limit state domain*  $\mathbb{T}_\varepsilon(\boldsymbol{\varepsilon})$ : compressive and tensile boundaries are considered for strain of steel and concrete, as in the classic ultimate limit state analysis.
2. *Elastic domain*  $\mathbb{T}_y(\boldsymbol{\varepsilon})$ : materials are assumed to be infinitely ductile, as usual in limit analysis of structures.

While the ultimate limit domain is usually employed in structural design, consistently with several code provisions, the Elastic Domain introduces, in general, a strong condition concerning ductility which does not fulfill code requirements. Nevertheless, it benefits of interesting properties so that its employment in computational tools could be more efficient than the ultimate limit domain.

### 2.1 Ultimate limit surface of RC beam sections accounting for strain limit

According to Eurocode’s prescriptions the axial strain of concrete is limited in compression by the value  $\varepsilon_{cu} < 0$ ; hence, the boundary of the domain collecting all admissible strain components is defined by

$$\partial\mathbb{E}_\boldsymbol{\varepsilon} = \left\{ \boldsymbol{\varepsilon} : \min_{\bar{\mathbf{x}} \in \Omega_c} \varepsilon_{11}(\boldsymbol{\varepsilon}, \bar{\mathbf{x}}) = \varepsilon_{cu} \right\} \tag{6a}$$

The set of stress resultants  $\partial\mathbb{T}_\varepsilon = \mathbf{t}[\boldsymbol{\varepsilon}, \bar{\mathbf{x}}]$ , associated with the admissible generalized strains  $\boldsymbol{\varepsilon}[\bar{\mathbf{x}}] \in \partial\mathbb{E}_\boldsymbol{\varepsilon}$  by means of (4), define the *ultimate limit state* (ULS) surface of the section which is used, in practical applications, to carry out the cross section strength checks.

As shown in [24], fixed a trial generalized strain  $\bar{\epsilon}_k$ , it can be shrunk or amplified in order to fulfill Eq. (6a) by means of a strain multiplier  $v_k$  given by

$$v_k = \max_{\mathbf{x} \in \Omega_c} \frac{\epsilon_{11}[\bar{\epsilon}_k, \bar{\mathbf{x}}]}{\epsilon_{cu}} \tag{6b}$$

hence, the normal resultants  $\mathbf{t}_{ek}$  on the ULS surface of the section, can be evaluated as a function of  $\epsilon_{cu}$  and the geometry of  $\Omega_c$  for the assigned  $\bar{\epsilon}_k$ , accordingly to Eq. (4), as

$$\mathbf{t}_{ek} = \mathbf{t}[\epsilon_k, \bar{\mathbf{x}}], \quad \forall k \text{ being } \epsilon_k = v_k \bar{\epsilon}_k \tag{6c}$$

An effective approach for the evaluation of the integrals on the right-hand side of Eq. (4) has been proposed in [24, 25], to which we refer readers for further details. Nevertheless, it must be emphasized that stress integrals are computed in closed-form as a functions of the position vectors  $\mathbf{x}_i$  of the  $n_v$  vertices of  $\Omega_c$  and of the values that the primitives of the function  $\sigma_c(\epsilon, \bar{\mathbf{x}})$  assume at these points.

Denoting as  $\mathbf{t}_d$  and  $\mathbf{t}_l$  the section forces associated with dead and live loads, respectively, capacity check consists in computing the multiplier  $\lambda$  fulfilling the condition:

$$\mathbf{t}_d + \lambda \mathbf{t}_l \in \partial \mathbb{T}_\epsilon \tag{6d}$$

thus assuming that only live loads can actually be increased by an amount measured by the positive scalar quantity  $\lambda$ .

As shown in [24], the computation of  $\lambda$  is not straightforward because the trial strain associated with section forces is in general unknown; hence, a line-search Newton–Raphson optimization procedure is required. Although the evaluation of the whole capacity surface is not required since it is sufficient to compute a single point only to fulfill the capacity check, this procedure turns out to be computationally demanding because it requires the computation of all stress integrals at each iteration of the optimization procedure.

### 2.2 Yield surface of infinitely ductile sections

In case of infinitely ductile constitutive laws for both concrete and steel, the computation of the limit domain, which has been exploited in [18, 21], is simpler and it turns out to be similar to the *stress blocks* approach widely employed in the past.

In particular, if a trial strain  $\epsilon_k$  is proportionally amplified in order to ideally drive the uniaxial strain  $\epsilon_{11}$  to infinity, then the uniaxial stress  $\sigma_c$  tends to its limit value  $f'_{cu}$  for all points belonging to the compressed region:

$$\lim_{\epsilon_{11}(\epsilon_k, \bar{\mathbf{x}}) \rightarrow -\infty} \sigma_c[\epsilon_{11}(\epsilon_k, \bar{\mathbf{x}})] = f'_{cu} \tag{7a}$$

while reinforcing bars reach either the tensile or compressive peak stress depending of their position with respect to the neutral axis defined by  $\epsilon_k$ :

$$\lim_{\epsilon_{11}(\epsilon_k, \bar{\mathbf{x}}_j) \rightarrow \pm\infty} \sigma_s[\epsilon_{11}(\epsilon_k, \bar{\mathbf{x}}_j)] = \pm f_{su,j} \tag{7b}$$

Eventually, the stress resultants are computed as:

$$\mathbf{t}_{yk} = \mathbf{t}_y(\epsilon_k) = \int_{\Omega_c} f'_{cu} \bar{\mathbf{x}} d\Omega + \sum_{j=1}^{n_r} f_{su,j} \bar{\mathbf{x}}_j \Omega_j \tag{7c}$$

where the first integral can be easily evaluated by the numerical procedure described in [21].

Limit values of the stress computed by Eq. (7c) can be directly used in limit and shakedown analyses since, as shown in [18], they represent the yield values associated with the plastic mechanism defined by direction  $\epsilon_k$ .

Specifically, the plastic mechanism corresponding to the generalized strain  $\epsilon_k$  is defined by the function:

$$\pi_{\mathbb{T}}(\epsilon_k) = \max \{ \mathbf{n}_k^T \mathbf{t} : \mathbf{t} \in \mathbb{T} \} \quad \text{with} \quad \mathbf{n}_k = \frac{\epsilon_k}{\|\epsilon_k\|} \tag{7d}$$

where  $\pi_{\mathbb{T}}(\epsilon_k)$  represents the signed distance from the origin of the hyperplane tangent to  $\mathbb{T}$  at the point with normal  $\mathbf{n}_k$ , see, e.g. Fig. 2.

The vector  $\mathbf{t}_{yk} \equiv \mathbf{t}_y(\epsilon_k) \in \partial \mathbb{T}$ , evaluated using Eq. (7c) and maximizing Eq. (7d), automatically satisfies the condition:

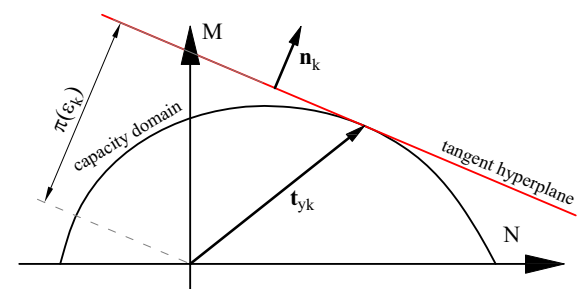


Fig. 2 Support function of the the elastic domain



$$\mathbf{n}_k^T(\mathbf{t}_{yk} - \mathbf{t}) \geq 0 \quad \forall \mathbf{t} \in \mathbb{T} \tag{7e}$$

The boundary  $\partial\mathbb{T}_y$  of the elastic domain  $\mathbb{T}_y$ , which is characterized by the condition  $\Phi[\boldsymbol{\varepsilon}, \mathbf{t}(\boldsymbol{\varepsilon})] = 0$ , will be named *yield surface*.

It is worth being emphasized that  $\pi_{\mathbb{T}}(\boldsymbol{\varepsilon}_k)$  represents the *support function* of  $\mathbb{T}_y$  and benefits of several algebraic features. In particular, as shown in [18] and [21], the unitary vector  $\mathbf{n}_k$ , normal to the tangent hyperplane at  $\mathbf{t}_y(\boldsymbol{\varepsilon}_k)$ , is parallel to the gradient of the overall trial strain  $\boldsymbol{\varepsilon}_k$  with respect to the plastic strain increment. For this reason, it is possible to establish a closed-form relationship between trial strain and limit stress.

### 2.3 Domain approximation by Minkowski sum of ellipsoids

The support function represents an analytical tool that can be conveniently used in approximating the elastic domain. Specifically, the *Minkowski sum of ellipsoids* is capable of defining  $n$ -dimensional surfaces by means of a superposition of ellipsoids [39].

To better illustrate its properties, let us consider a single ellipsoid defined in the generalized stress space and centered at the origin. Its canonical equation is:

$$\mathbf{M}\mathbf{t} \cdot \mathbf{t} = 1 \tag{8a}$$

where  $\mathbf{t}$  is a generic point of the ellipsoid,  $\mathbf{M}$  is a positive-definite  $3 \times 3$  square matrix and operator  $\cdot$  denotes scalar product.

It can be proved that the *support function* of the ellipsoid, that can be interpreted as the distance of the tangent hyperplane at  $\mathbf{t}$  from the origin, is defined by

$$\pi(\mathbf{t}) = [\boldsymbol{\alpha}(\mathbf{t})^T \mathbf{M}^{-1} \boldsymbol{\alpha}(\mathbf{t})]^{0.5} = [\mathbf{M}^{-1} \boldsymbol{\alpha}(\mathbf{t}) \cdot \boldsymbol{\alpha}(\mathbf{t})]^{0.5} \tag{8b}$$

where  $\boldsymbol{\alpha}$  is the unit vector normal to the tangent hyperplane.

If the matrix  $\mathbf{M}$  is known, the vector  $\boldsymbol{\alpha}$  can be used as a parameter for computing any point of the ellipsoids by the relationship:

$$\mathbf{t}(\boldsymbol{\alpha}) = \frac{\mathbf{M}^{-1} \boldsymbol{\alpha}}{[\boldsymbol{\alpha}^T \mathbf{M}^{-1} \boldsymbol{\alpha}]^{0.5}} \tag{8c}$$

Complex domains are properly approximated by the superposition of several ellipsoids. Specifically, denoting as  $\mathbf{M}_i, i = 1, \dots, m$ , the canonic matrices of

$m$  ellipsoids and as  $\mathbf{t}_0$  the vector locating the domain center with respect to the origin, the Minkowski sum is defined as:

$$\mathbf{t}(\boldsymbol{\alpha}) = \mathbf{t}_0 + \sum_{i=1}^m \frac{\mathbf{M}_i^{-1} \boldsymbol{\alpha}}{[\boldsymbol{\alpha}^T \mathbf{M}_i^{-1} \boldsymbol{\alpha}]^{0.5}} \tag{8d}$$

Figure 3 shows an illustrative Minkowski sum approximating the elastic domain of a reinforced concrete cross section; specifically, blue bullets are the points of the original domain while the white surface represents its approximation obtained by the Minkowski sum of the red, green and blue ellipsoids.

Formulation of Eq. (8d) is particularly efficient for computational implementations since the evaluation of the generalized stress is performed by bilinear operations regardless of the complexity of the domain to be approximated. Nevertheless, the Minkowski sum is an efficient tool as long as it is possible to determine the canonical matrices  $\mathbf{M}_i$ . To this end, the higher is  $m$ , the more accurate would be the sum; although, a large number of ellipsoid makes the identification of matrices  $\mathbf{M}_i$  more difficult. Nevertheless, it has been shown in [18] that, in case of reinforced concrete yield surfaces, three ellipsoids usually provide a good approximation.

A further issue concerns the calibration of the Minkowski sum for a discrete number of points  $\mathbf{t}_j$ . Identification of matrices  $\mathbf{M}_i$  is usually performed by optimization algorithms whose convergence is almost

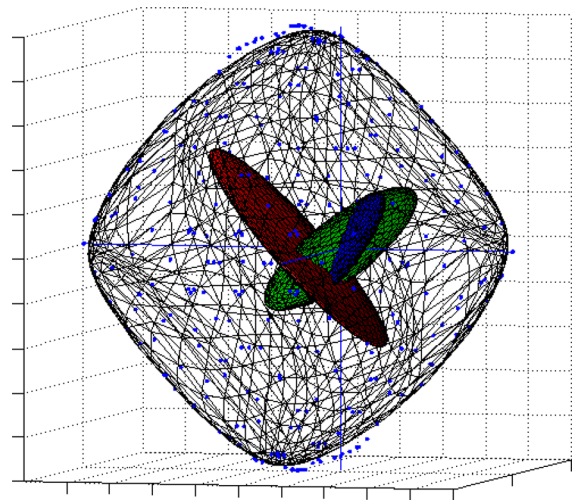


Fig. 3 Illustrative 3-ellipsoids Minkowski sum

impossible if normal vectors  $\alpha_j$  at points  $\mathbf{t}_j$  are not known.

For this reason, support functions of the elastic domain, defined in Eq. (8b), make the Minkowski sum calibration straightforward. On the contrary, a similar approximation for the ULS domain, although possible, requires a significant computational burden in order to determine the normals by finite differences.

The computational convenience of the described procedure encourages the purpose of replacing the ultimate limit state domain with the elastic one. However, for the reasons detailed in Sect. 4, the elastic domain generally yields unconservative results unless it is evaluated by neglecting the external cover.

### 3 Confinement effects on the behavior of reinforced concrete frame cross sections

As previously stated, structural codes prescribe strain limits to concrete and steel in order to define the ultimate limit state of cross sections. In general, each cross-section can be idealized as the superposition of discrete reinforcement bars, the concrete confined core (enclosed by the stirrups) and the external unconfined cover. Assuming materials to be homogeneous and following Eurocode 2 provisions, the cross-section ULS depends on the attainment of the ultimate strain either in the most stressed steel bar or at one of the vertices of the concrete cover.

However, the actual behavior of r.c. cross-sections can be sensibly different from the standard code idealization because of two aspects:

1. the ultimate strain of the core concrete can be sensibly greater than the limit imposed by codes because of the confinement effect;
2. concrete cover is usually strongly damaged by seismic actions although the cross-section still preserves a significant strength.

The comparisons illustrated below aim to take into account these two issues and amount to computing the bending moment–curvature curves for a fixed value of the axial force.

Investigations presented in this section are relevant to the cross section shown in Fig. 4 subject to uniaxial and biaxial bending. The section has size 300 mm × 500 mm, is endowed with strength concrete  $f_{cd} =$

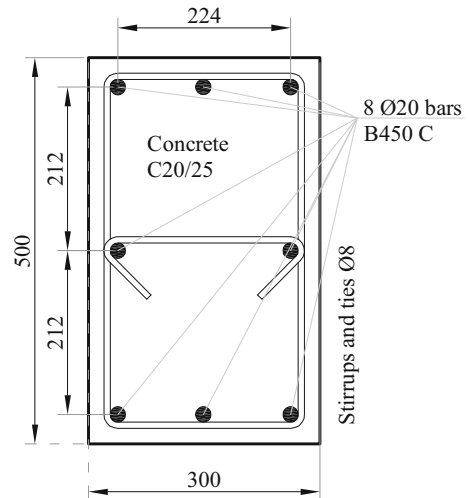


Fig. 4 Rectangular cross-section geometry

8.3 MPa, corresponding to an ultimate limit state strain  $\epsilon_{cu}^{SLU} = 0.0035$ , and is reinforced by 8Ø20 mm bars (4 at corners and 4 at midpoints of each side) having strength  $f_{yd} = 450$  MPa. Transversal reinforcement is composed of a rectangular stirrup and a cross tie parallel to the section width; both have diameter of 8 mm and spacing of 150 mm.

Specifically, three analysis typologies have been carried out. The first typology aims to accurately model the actual behavior of the cross section by assuming the Karthik–Mander (KM) model [13] indifferently for concrete core and unconfined cover; core confinement has been considered by conveniently calibrating the constitutive parameters.

In particular, denoting by  $f'_{c0}$  the characteristic compressive strength of the unconfined concrete, the relevant strength  $f'_{cc}$  of the confined concrete is evaluated as

$$f'_{cc} = f'_{c0} \left( -1.254 + 2.254 \sqrt{1 + 7.94 \frac{f'_l}{f'_{c0}}} - 2 \frac{f'_l}{f'_{c0}} \right) \tag{9}$$

while the associated strain  $\epsilon_{cc}$  can be evaluated as

$$\epsilon_{cc} = \epsilon_{c0} \left[ 1 + 5 \left( \frac{f'_{cc}}{f'_{c0}} - 1 \right) \right] \tag{10}$$

The quantity  $f'_l$  depends on the transverse reinforcement by means of the expression

$$f'_l = \frac{1}{2}k_e\rho_s f_{yh} \tag{11}$$

where  $k_e$  depends on the section shape [23],  $\rho_s$  is the relevant volume ratio with respect to the confined concrete core and  $f_{yh}$  is the corresponding yielding strength. Such parameters are then used to express the stress–strain law of confined concrete

$$\sigma_{11}(\epsilon_{11}) = \begin{cases} f'_{cc}[1 - (1 - x)^n] & 0 \leq x \leq 1 \\ f'_{cc} - \frac{f'_{cc} - f_{cu}}{x_u - 1}(x - 1) & 1 \leq x \leq x_u \\ f_{cu} \frac{x - x_f}{x_u - x_f} & x_u \leq x \leq x_f \end{cases} \tag{12}$$

where  $\epsilon_{11}$  is the longitudinal compressive strain of concrete, evaluated in our case according to Eq. (2),  $x = \epsilon_{11}/\epsilon_{cc}$ ,  $x_u = \epsilon_{cu}/\epsilon_{cc}$  and  $x_f = \epsilon_f/\epsilon_{cc}$ . Moreover,  $\epsilon_{cc}$  represents the peak strain,  $\epsilon_{cu}$  the ultimate strain,  $\epsilon_f$  the failure strain, exponent  $n = E_c\epsilon_{cc}$  and elasticity modulus  $E_c = 5000\sqrt{f'_{c0}}$  MPa.

The constitutive law (12) holds as long as the compressive strain of concrete  $\epsilon_{11}$  is lower than the limit value  $\epsilon_{cu}$ ; this last one, in turn, is influenced by confinement. Actually, as shown in [23],  $\epsilon_{cu}$  has to be evaluated on the basis of an energy balance, as the concrete longitudinal strain corresponding to the first fracture of transverse reinforcement.

An alternative formulation, providing an accurate estimation of  $\epsilon_{cu}$  and adopted in the sequel, has been suggested in [5, 33]

$$\epsilon_{cu} = 0.004 + 1.4 \frac{\rho_s f_{yh} \epsilon_{su}}{f'_{cc}}, \quad \epsilon_{su} = 0.06 \tag{13}$$

where  $\rho_s, f_{yh}$  and  $\gamma$  are the volume ratio of the transversal reinforcements, the corresponding yield strength and  $\gamma = k_e f_{yh}/f'_{c0}$ , respectively.

In order to show the dependence of  $\epsilon_{cu}$  upon the confinement rate, Fig. 5 shows the ultimate strain of the rectangular cross section shown in Fig. 1 depending on the distance between two consecutive stirrups computed by following the procedure introduced by Mander et al. [23] and the one proposed by Priesley et al. [33] summarized in Eq. (13).

The softening branch of the confined concrete stress–strain curve, i.e. the one between  $\epsilon_{cc}$  and  $\epsilon_{cu}$ , terminates at the ultimate strength of confined

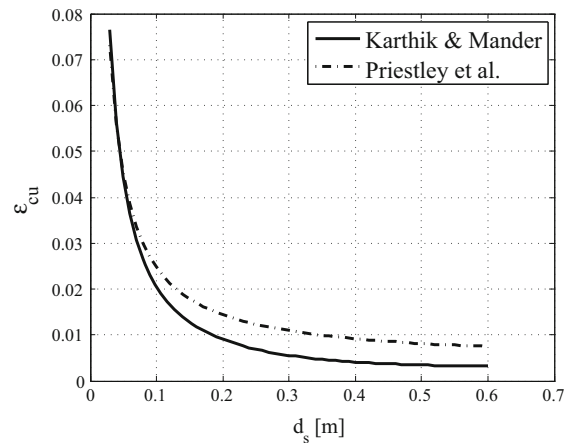


**Fig. 5** Dependence of ultimate strain  $\epsilon_{cu}$  of confined concrete upon longitudinal distance  $d_s$  between two consecutive stirrups

concrete  $f'_{cu}$  see, e.g. Fig. 6. It is evaluated from (12) as the stress corresponding to the longitudinal strain  $\epsilon_c = \epsilon_{cu}$ .

In order to investigate the influence of the concrete cover on the cross section strength, a second typology of analyses has been carried out by neglecting the cover contribution and adopting the KM model for confined concrete.

Finally, the third typology models the concrete core by a parabola–rectangle constitutive model whose parameters are calibrated to account for confinement while concrete cover is neglected.

In particular the assumed constitutive law is defined by

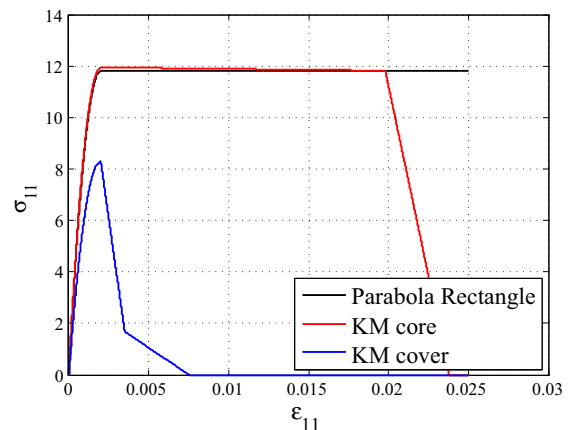


**Fig. 6** Stress–strain relationships of the Kurtik–Mander and parabola–rectangle constitutive models



$$\sigma_{11}(\epsilon_{11}) = \begin{cases} 0 & \text{if } 0 < \epsilon_{11} \\ a\epsilon_{11} + b\epsilon_{11}^2 & \text{if } \epsilon_{cp} < \epsilon_{11} < 0 \\ \sigma_{cu} & \text{if } \epsilon_{cu} < \epsilon_{11} < \epsilon_{cc} \\ 0 & \text{if } \epsilon_{11} < \epsilon_{cu} \end{cases} \quad (14)$$

where  $\sigma_{11}$  denotes concrete stress,  $\epsilon_{cc}$  is the yield strain and  $\epsilon_{cu}$  is the ultimate strain. Coefficients  $a$  and  $b$  in Eq. (14) are given by  $a = -1000\sigma_{cu}$  and  $b = 250a$  where peak stress  $\sigma_{cu} = -0.85f_{ck}/1.6$  is defined by means of the concrete characteristic compression strength  $f_{ck}$ .

The Kurtik–Mander and parabola–rectangle constitutive models are shown comparatively in Fig. 6. For the above mentioned analysis typologies, two ultimate limit states have been defined for both concrete core and unconfined cover as the attainment of the same value of ultimate strain.

By exploiting the relationships reported in Equations (9)–(13), the reinforcement set-up in Fig. 4 makes confined concrete to attain  $f'_{cc} = 11.947$  MPa as peak stress,  $f'_{cu} = 11.817$  MPa as ultimate strength and  $\epsilon_{cu} = 0.0198$  as ultimate strain.

Moment–curvature curves of the analyzed cross section are reported in Fig. 7a, b. Specifically, blue and red curves correspond to the Karthik–Mander concrete constitutive model [13] while the black one is associated with the concrete parabola–rectangle stress–strain relationship. Contribution of the concrete cover has been taken into account for the blue curve

only. Moreover, the attainment of the ultimate limit strain at the concrete cover and at the section core are indicated by bullet markers.

Both the uniaxial and biaxial tests have been carried out by proportionally increasing the curvature and computing the total bending moment as internal force in equilibrium with the assigned curvature. In the case of uniaxial bending, illustrated in Fig. 7a, curvature has been assigned about the horizontal axis while in the case of biaxial bending, see, e.g. Fig. 7b, curvature is assigned by means of two equal components acting about both axes so that the neutral axis turns out to be rotated of  $\pi/4$  with respect to the horizontal axis.

The presence of the unconfined concrete cover only influences the initial part of the curves, while the plateau that characterizes all curves corresponds to approximately the same value of bending moment.

Additionally, since the beneficial effect of confinement is such that the corresponding stress–strain law is characterized by a very low softening, the curvature values for which the parabola–rectangle constitutive law over-estimates the bending moment with respect to the Karthik–Mander curves are very high and, in the examples illustrated in the sequel, greater than the value corresponding to the attainment of the ultimate limit states both in the core and the cover. For this reason, the parabola–rectangle constitutive law well predicts the ultimate value of bending moment.

This phenomenon is clarified by Figs. 8 and 9, where the stress distributions corresponding to the core ultimate limit states (identified by red bullets in

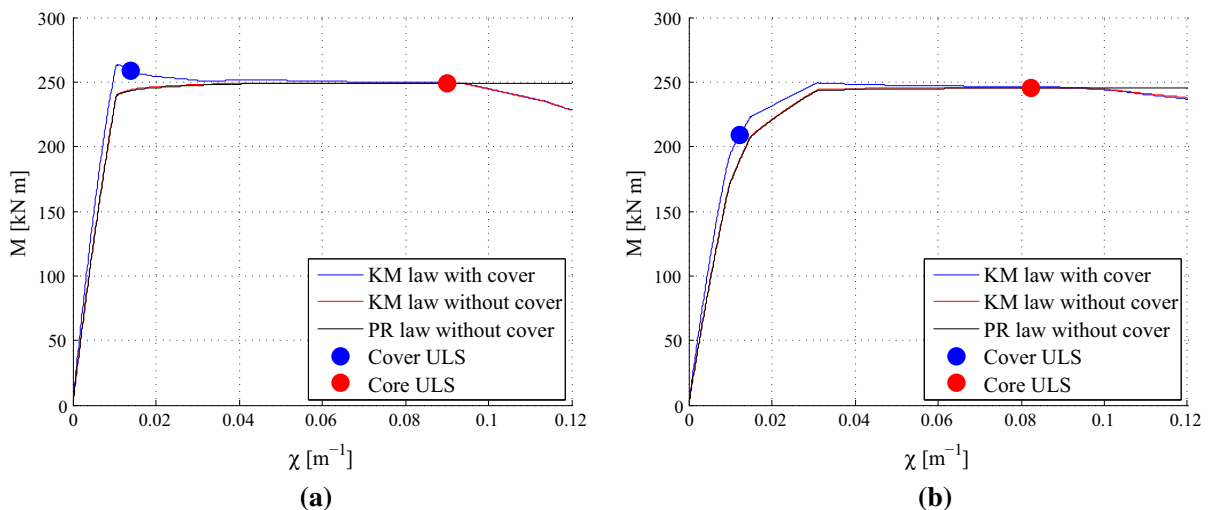
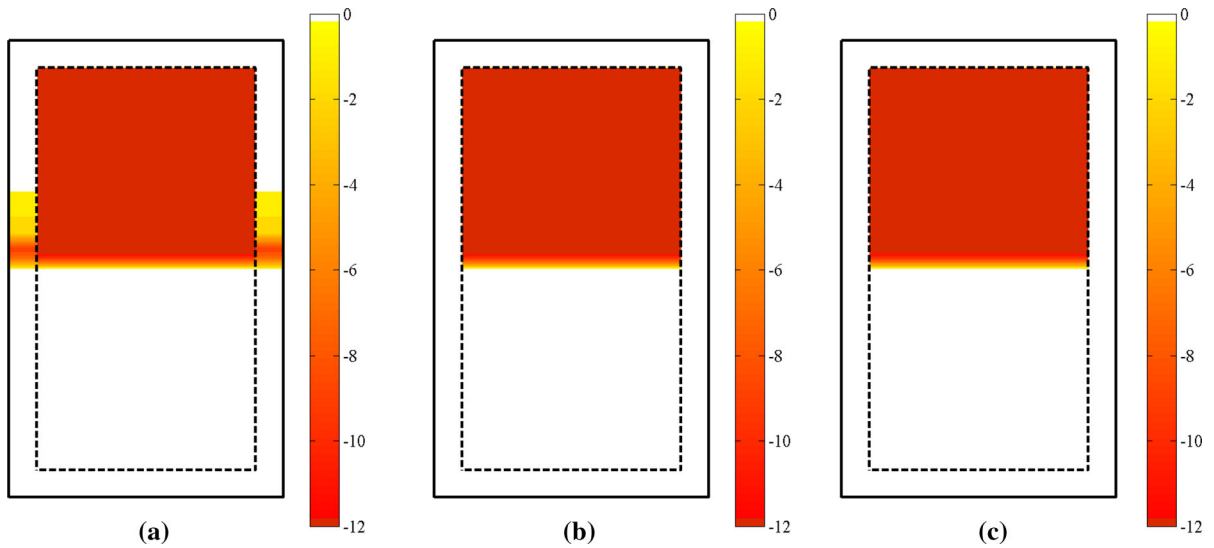
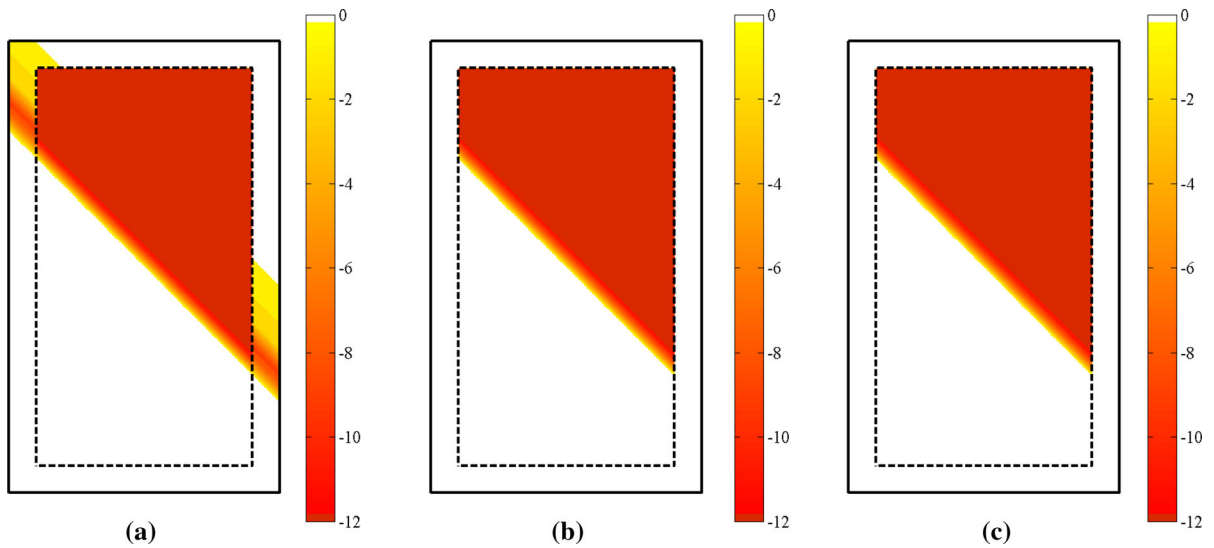


Fig. 7 Bending moment: curvature curves. **a** Uniaxial bending and **b** biaxial bending. (Color figure online)



**Fig. 8** Normal stress (MPa) distribution at the core ULS—uniaxial bending. **a** KM law with cover, **b** KM law without cover and **c** PR law without cover



**Fig. 9** Normal stress (MPa) distribution at the core ULS—biaxial bending. **a** KM law with cover, **b** KM law without cover and **c** PR law without cover

Figs. 7a, b) are illustrated for all the considered constitutive relationships. In particular, Fig. 8 refers to uniaxial bending while Fig. 9 corresponds to biaxial bending. All stress distributions have been plotted in order to attain compression at the top of the section.

Considering the Karthik–Mander concrete constitutive model, a comparison between Fig. 8a, b shows how the contribution of the unconfined core is quite limited. Moreover, the stress distribution concerning

the cover is clustered close to the neutral axis since its far region has reached the collapse in the sense that stress is zero.

The very same phenomenon is shown by comparing Fig. 9a, b in case of biaxial bending where the right-top corner, although compressed, has zero stress because ultimate limit state has been attained in the concrete cover.

Such comparisons show how the contribution of the unconfined cover to the global strength of the cross section is almost negligible. For this reason, it is reasonable to neglect the presence of the cover when carrying out ULS analyses by adopting either the KM or the PR model.

Further comparisons between Fig. 8b, c, in case of uniaxial bending, and Fig. 9b, c, in case of biaxial bending, show how the stress distributions computed by the Karthik–Mander concrete constitutive model (Figs. 8b, 9b) and the parabola–rectangle law (Figs. 8c, 9c) present almost negligible differences. This is due to the peculiar softening phase of the Karthik–Mander relationship: since the confinement ensures a very low softening tangent stiffness, the curve is almost coincident with the parabola–rectangle plateau.

Influence of ultimate limit states on the capacity of the cross section depend on the kind of internal force that is taken into account. Specifically, in case of uniaxial bending, bending moment–curvature relationship presents a well-defined peak and both the concrete core and cover attain their respective ultimate limit states after that the maximum value of the bending moment has been attained.

On the contrary, in the case of biaxial bending, the bending moment–curvature relationship is monotonically non-decreasing and ultimate limit states for concrete core and cover correspond to sensibly different values of the bending moment.

In other words biaxial bending curves in Fig. 7 show how the attainment of the ultimate limit strain of cover does not correspond to the actual bending strength of the section. Conversely, the limit value of the bending moment is well represented by the attainment of the ultimate limit strain at the section core.

The previous results naturally prompt some considerations related to the everlasting conflict between strength and ductility of structural elements. Actually, one is induced to think that neglecting concrete cover is a conservative approach since a certain amount of material is disregarded.

However, this spontaneous path of reasoning can contrast with code prescriptions since concrete cover is distributed along the outer part of the section where strains are likely to attain the utmost values since the relevant points are the farthest ones from the neutral axis.

Considering also that concrete cover is characterized by a lower value of the ultimate strain limit, since concrete is unconfined, one infers that ignoring concrete cover in the section analysis can lead to unconservative results, as Fig. 7 suggests, since the ultimate limit state in presence of cover (blue bullet) is attained well before than the analogous condition when concrete cover is ignored (red bullet).

Nevertheless we state that nonlinear analysis of r.c. structures has to be carried out by neglecting concrete cover basically for two reasons. First, ULS analysis of the r.c. sections, and the relevant value of the ultimate strain, have been calibrated in Eurocode 2 for uniaxial bending, a situation that is realistic only for beams. In passing we notice from Fig. 7b that the ultimate bending moment in presence of biaxial bending is not properly evaluated when conventional ULS analysis is carried out.

A second reason for ignoring concrete cover in nonlinear sectional analysis lies in the fact that Eurocodes prescriptions in terms of reinforced bars layout and quantity, as well as in terms of constructive details, are explicitly established with the main purpose of ensuring confinement and ductile behavior of reinforced concrete. In turns this is consistent with design methodology in earthquake engineering according to which the value of the structural factor increases for a more pronounced post-yield behavior of structural members. Coherently with such assumptions, analysis has to contemplate the complete damage of concrete cover, whose collapse is fragile, while the core section preserves a significant strength.

The previous considerations validate the use of the parabola–rectangle constitutive law, whose parameters are calibrated to account for confinement and section ductility, yet keeping the ultimate strain at the value  $\epsilon_{cu} = 0.0035$ , prescribed by Eurocode 2, for the evaluation of the ultimate strength of confined reinforced concrete sections. To this end, since the cover can collapse before the attainment of the cross section core ultimate limit state, its contribution shall be neglected.

#### 4 Comparison between the ULS surface and the yield surface

As anticipated in the introduction, this work aims to investigate the chance of surrogating the nonlinear

response of reinforced concrete cross sections by means of the elastic domain.

For brevity, we discuss the results of just two cross sections although in our study we have analyzed several kinds of sections, differing both for geometry and dimensions. Numerical experiments have shown that the results illustrated in the sequel hold independently from the section geometry, reinforcement layout and constitutive properties. Specifically, the first cross section has been introduced in Fig. 4 while the results of further analyses concern the L-shaped cross section represented in Fig. 10.

Steel reinforcement bars and unconfined concrete have the same constitutive parameters as the ones introduced in Sect. 3, while parameters of the confined region are summarized in Table 1. Specifically, confined concrete peak stress  $f'_{cc}$  is evaluated by considering the stirrups and ties, of diameter  $\phi$  8 mm and setup depicted in Fig. 10, having spacing equal to 150 mm.

It is worth to be emphasized that parameter  $k_e$  of Eq. (11), depending on the section shape [23], is characterized for rectangular or circular sections only. For this reason,  $f'_{cc}$  of the L-shaped section has been computed separately for each rectangular wing and the relevant results are summarized in Table 1. Moreover, in order to define a unique constitutive model for

**Table 1** Mechanical properties of the L-shaped cross section

| $R_{ck}$ | $f'_{c0}$ | Wing A          |           | Wing B          |           |
|----------|-----------|-----------------|-----------|-----------------|-----------|
|          |           | $\epsilon_{cu}$ | $f'_{cu}$ | $\epsilon_{cu}$ | $f'_{cu}$ |
| 15       | 8.300     | 0.0178          | 10.844    | 0.01781         | 11.09595  |
| 30       | 16.600    | 0.0106          | 19.132    | 0.010656        | 19.441320 |

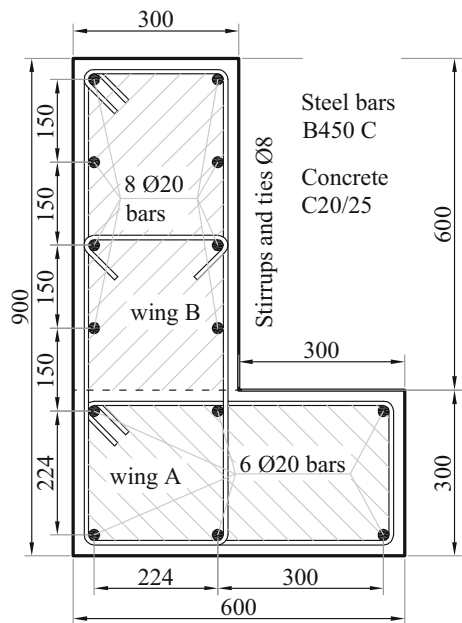
confined concrete, it has been assumed  $f'_{cc} = 19.132$  MPa.

Figure 11 shows the ULS surface and the yield surface associated with the rectangular cross section depicted in Fig. 4. The contribution of the unconfined concrete cover has been neglected in computations, according to the conclusions drawn in Sect. 3.

All surfaces have been obtained by considering a value of the concrete strength equal to the ultimate strength of confined concrete, while increasing values of ultimate strain have been considered for each comparison.

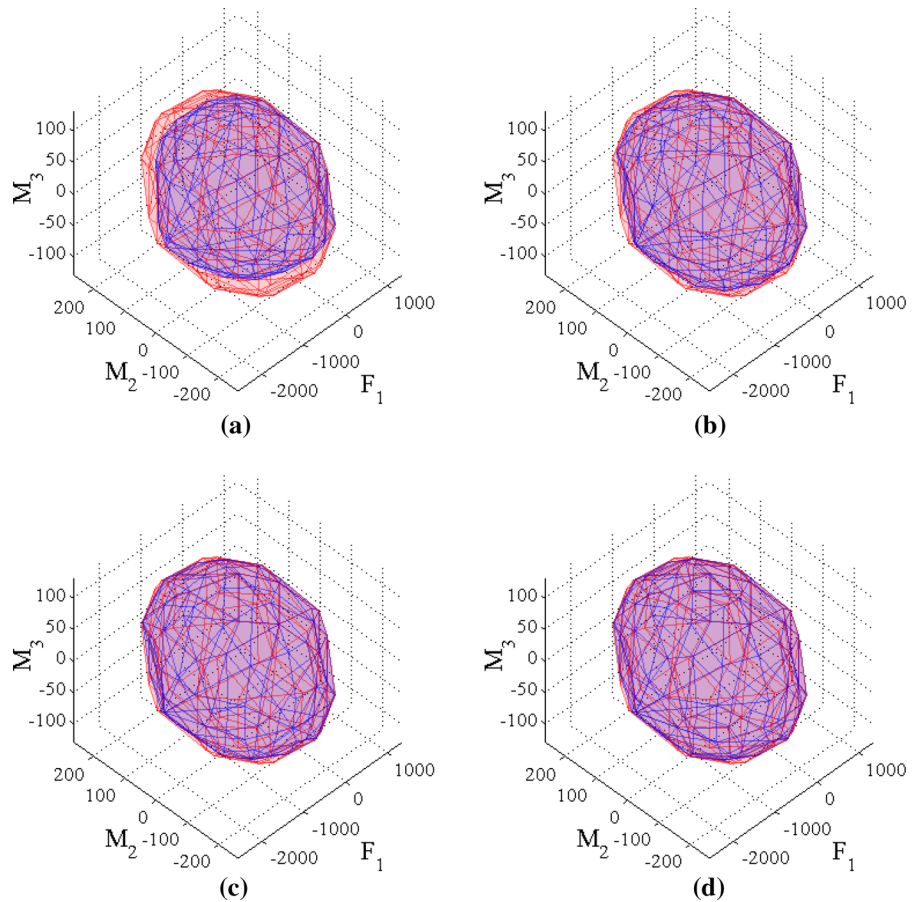
A qualitative examination of the two surfaces clearly shows how the ULS surface tends to the yield surface as the ultimate value of the strain increases. This is expected because, as long as the maximum value of the allowed compressive strain increases, the internal forces are computed for a generalized strain which becomes closer to the infinite ductility condition. Moreover, it can be observed, particularly in Fig. 11a, that the higher discrepancies are attained for compressive values of the axial force. This makes sense since the compressed region of the ULS domain correspond to stress states for which the cross section attains the compressive limit state in concrete. On the contrary, for tensile axial forces, for which the ultimate limit state is ruled by steel, the greater ductility of the material makes the points of the ULS surface to be closer to the yield surface.

A similar behavior can be observed by considering Fig. 12a for the L-shaped cross section in Fig. 10. It is worth to be emphasized that asymmetry of the cross section influences the shape of both domains. Again, the higher discrepancies between the limit surfaces are observed for compressive values of the axial force; moreover, the effect of confinement on concrete ductility is sufficient to make the ultimate limit surface of the section almost indistinguishable from the relevant yield surface, as already observed for the rectangular section.



**Fig. 10** L-shaped cross section. Geometry and data

**Fig. 11** Comparison between the yield surface (red) and the ultimate limit state surfaces (blue) of the rectangular cross section of Fig. 4 for increasing values of ultimate strain of concrete. Concrete cover neglected. **a**  $\epsilon_{cu} = 0.0035$ . **b**  $\epsilon_{cu} = 0.0060$ . **c**  $\epsilon_{cu} = 0.0085$ . **d**  $\epsilon_{cu} = 0.0110$ . (Color figure online)



Such qualitative comparisons, although encouraging, are not yet capable of providing reliable engineering information since it is necessary to numerically analyze the difference between the yield and ultimate limit domain. This will be addressed in the following two subsections by focusing on two different aspects of the stress response. Specifically, while Sect. 4.1 focuses on the distance between the two boundary surfaces expressed in terms of internal forces, Sect. 4.2 investigates the response difference associated with the same strain mechanism.

#### 4.1 Comparison in terms of internal forces

The first comparison between the ULS surface and the yield surface, defined in Sects. 2.1 and 2.2 respectively, analyzes the differences in terms of stress resultants.

These analyses investigate about the role played by the ultimate limit strain value assumed for concrete on

the strength values of the section forces. In this respect it is expected that the ultimate limit surface asymptotically tends to the yield surface as the ultimate value of the strain is increased. In particular, this section aims to show that, considering confinement degrees commonly experienced in real structures, the yield surface approximates, with sufficient accuracy, the ULS surface in all possible directions.

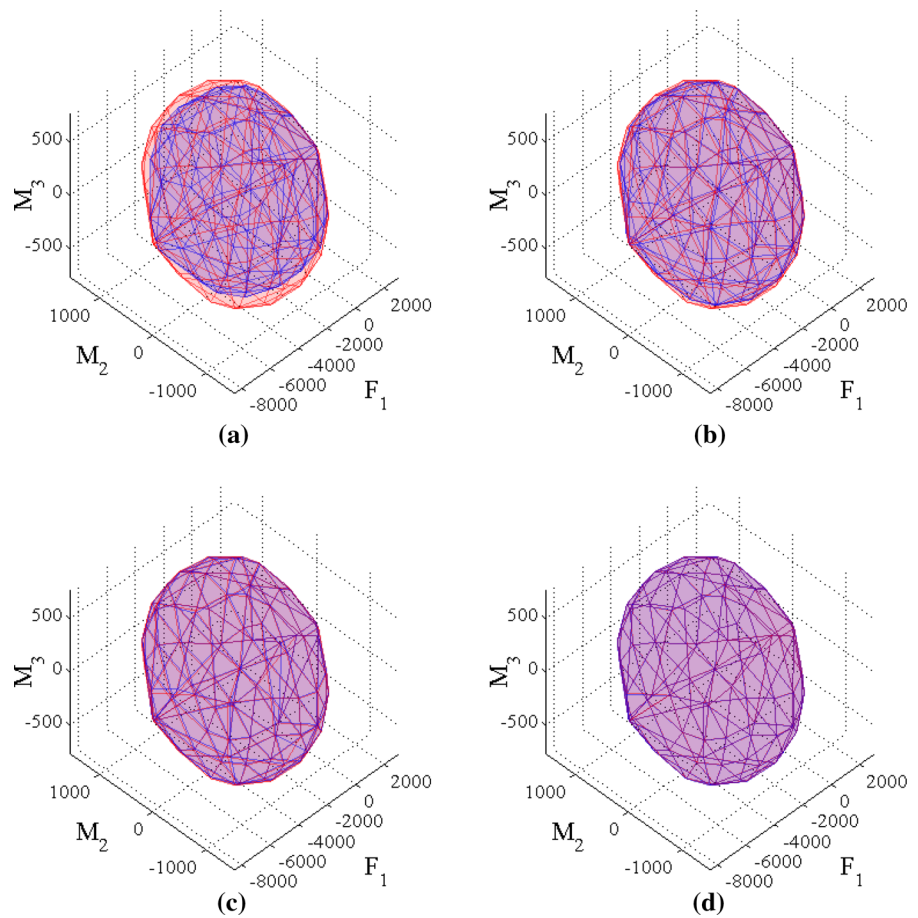
For brevity, we discuss the results of the two cross sections already considered in Sect. 4.2, specifically, the rectangular section depicted in Fig. 4 and the L-shaped one depicted in Fig. 10.

A numerical comparison between the surfaces can be carried out by computing the relative error defined as:

$$\mathcal{E}(\mathbf{t}_y[\epsilon_k]) = \min \left[ \frac{\|\mathbf{t}_\epsilon - \mathbf{t}_y[\epsilon_k]\|}{\|\mathbf{t}_\epsilon\|} \right] \tag{15}$$

where  $\mathbf{t}_y[\epsilon_k]$  is the points belonging to the yield surface corresponding to a generalized strain  $\epsilon_k$  while  $\mathbf{t}_\epsilon$  is a

**Fig. 12** Comparison between the yield surface (red) and the ultimate limit state surfaces (blue) of the L-shaped cross section of Fig. 10 for increasing values of ultimate strain of concrete. Concrete cover neglected. **a**  $\epsilon_{cu} = 0.0035$ . **b**  $\epsilon_{cu} = 0.0060$ . **c**  $\epsilon_{cu} = 0.0085$ . **d**  $\epsilon_{cu} = 0.0110$ . (Color figure online)



generical point belonging to the ultimate limit surface. In this sense the error is defined as the ratio of the distance between a point belonging to the yield surface  $\mathbf{t}_y[\epsilon_k]$  and the point  $\mathbf{t}_\epsilon$  belonging to the ultimate limit surface closest to  $\mathbf{t}_y[\epsilon_k]$ , points representative of sets of internal forces associated with the same strain value, and the norm of the internal forces vector belonging to the ultimate limit surface.

In order to provide a qualitative idea of the error distribution, Figs. 15 and 16 report error colormaps plotted on the limit domains.

It can be observed how the greatest error is strongly influenced by the axial force. In particular, error is clustered at the edge of the compressive regions and tend to decrease for lower axial forces.

This is expected in the light of the considerations developed in Sect. 3. In fact, in case of high compressive axial forces, section would likely attain concrete ultimate limit state for which it is significant the discrepancy between the elastic domain (with

infinite ductile behavior) and the ULS domain (with limited ultimate strains). Attainment of the ultimate limit state for small values of the generalized strain is indicative of the fact that the stress has not reached the peak value of the constitutive model over a large region of the cross section.

On the contrary, regions with tensile axial forces correspond to the attainment of steel ultimate limit state and the cross section exhibits a greater ductility; in this case stress reaches the yield value over a large region of the cross section so that stress resultants turn out to be closer to the values computed in case of infinite ductility.

It is also interesting to notice that errors affecting the compressive region of the limit surfaces are in inverse proportionality with respect to the concrete ultimate strain. Specifically, for the rectangular section, in case of  $\epsilon_{cu} = 0.0035$ , shown in Fig. 15a, error peaks are significant and concern almost the whole compressive half of the surface. As  $\epsilon_{cu}$  assumes greater



values, error tends to decrease and, in case of  $\epsilon_{cu} = 0.0110$  (Fig. 15b), it turns out to be smaller than 5%.

Concerning the L-shaped section, error colormaps plotted in Fig. 16 present higher errors. In particular, in case of  $\epsilon_{cu} = 0.0035$  error is clustered on the compressive region of the domain; such a phenomenon is expected since such a discrepancy can be observed already in Fig. 12a. Moreover, for  $\epsilon_{cu} \geq 0.0060$ , the error is clustered on an oblique wake which approximately follows the plane  $M_2 = M_3$ . These points correspond to internal forces for which compressive ultimate limit state is attained either at the corner of the cross section or at the ends of the wings.

A quantitative summary of the error trend, computed for all the considered cross sections, is reported in Tables 2 and 3 where peak and average error are reported as function of the ultimate strain for the rectangular and L-shaped section, respectively. It is worth being emphasized how, for the rectangular section, the average error results less than 3% even for  $\epsilon_{cu} = 0.0035$  that corresponds to the compressive ultimate limit state of unconfined concrete. As expected, higher values of the ultimate strain correspond to lower error averages since these last ones result less than 1% already for  $\epsilon_{cu} = 0.0085$ .

On the contrary, peak values of the error exhibits a more erratic behavior; in particular, its trend is not monothonic with respect to the ultimate strain. Nevertheless, this drawback does not affect a substantial equivalence between the domains at least in an average sense: but for the case of  $\epsilon_{cu} = 0.0035$ , the peak results lower than 5%.

The error computed for the L-shaped cross section, reported in Table 3, presents a similar trend and slightly higher values with respect to the rectangular section. In particular, the average error becomes less than 1% for  $\epsilon_{cu} = 0.0085$ .

It should be emphasized that, following the procedure introduced by Mander et al. [23] and Priesley et al. [33] and observing Fig. 5, the ultimate strain

**Table 2** Relative error between yield and ultimate limit state surfaces: rectangular section in Fig. 4

| $\epsilon_{cu}$ | $\mathcal{E}_{peak}$ | $\mathcal{E}_{avg}$ |
|-----------------|----------------------|---------------------|
| 0.0035          | 0.1022               | 0.0259              |
| 0.0060          | 0.0540               | 0.0099              |
| 0.0085          | 0.0333               | 0.0052              |
| 0.0110          | 0.0417               | 0.0042              |

**Table 3** Relative error between yield and ultimate limit state surfaces: L-shaped section in Fig. 10

| $\epsilon_{cu}$ | $\mathcal{E}_{peak}$ | $\mathcal{E}_{avg}$ |
|-----------------|----------------------|---------------------|
| 0.0035          | 0.1040               | 0.0304              |
| 0.0060          | 0.0669               | 0.0138              |
| 0.0085          | 0.0592               | 0.0097              |
| 0.0110          | 0.0533               | 0.0079              |

value  $\epsilon_{cu} = 0.0085$  is reached with stirrups distanced at  $d_s = 0.2$  m which is a far higher value than the stirrup spacings usually required by standard codes for the most stressed frame regions, typically the nodes.

The previous comparisons show encouraging results since a reasonable matching between the elastic and ultimate limit state domains can be appreciated. Moreover, the difference between the relevant boundaries becomes reasonably small for values of  $\epsilon_{cu}$  assumed as typical ultimate limit strain of ordinary confined concrete. For this reason, both definitions of limit surfaces can be reasonably used without distinction in practical applications.

#### 4.2 Comparison in terms of strain mechanisms

A further comparison between the yield and the ultimate limit state surface concerns the values of the generalized forces obtained for a set of strain mechanisms. Its purpose is to investigate the chance of surrogating the nonlinear response of cross sections in performing path-following analyses by an elastic-perfectly plastic behavior of the section. To this end, it is necessary to compare the responses in terms of generalized stresses for given values of the generalized strains.

In particular, fixed a set of strain mechanisms  $\epsilon_k$ , the generalized stresses  $\mathbf{t}_y[\epsilon_k]$  and  $\mathbf{t}_\epsilon[\epsilon_k, \epsilon_{cu}]$  are computed for the elastic and the ultimate limit state domain, respectively:

$$\mathbf{t}_y[\epsilon_k] = \begin{bmatrix} F_{1,y}(\epsilon_k) \\ M_{2,y}(\epsilon_k) \\ M_{3,y}(\epsilon_k) \end{bmatrix}; \tag{16}$$

$$\mathbf{t}_\epsilon[\epsilon_k, \epsilon_{cu}] = \begin{bmatrix} F_{1,\epsilon}(\epsilon_k, \epsilon_{cu}) \\ M_{2,\epsilon}(\epsilon_k, \epsilon_{cu}) \\ M_{3,\epsilon}(\epsilon_k, \epsilon_{cu}) \end{bmatrix} \tag{17}$$

Figure 13 shows the projection of the domains on the  $F_1$ – $M_3$  plane computed with a value of the ultimate

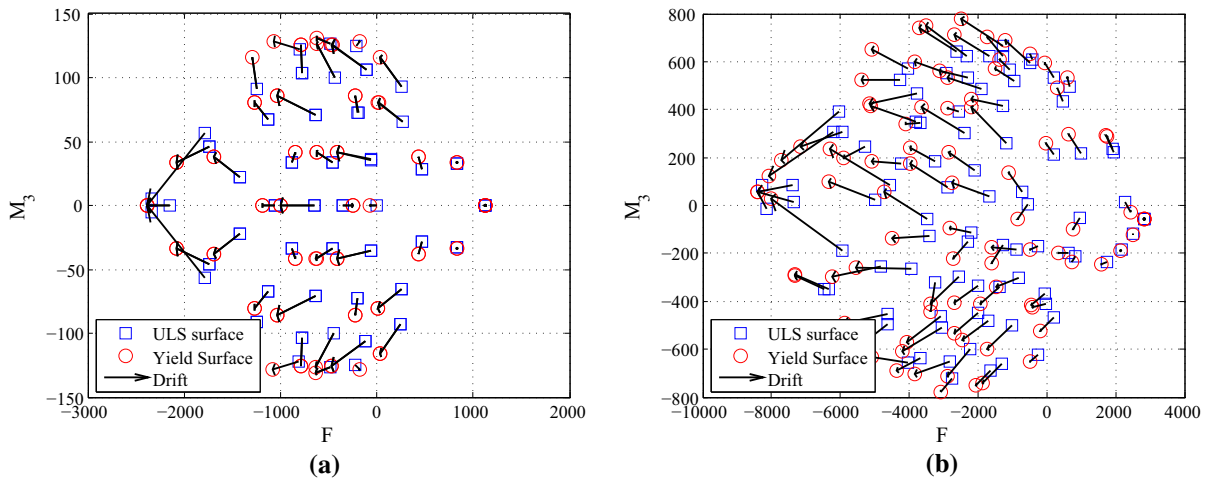


**Fig. 13** Projection of the domain drift for  $\epsilon_{cu} = 0.0035$ . **a** Rectangular section in Fig. 4 and **b** L-shaped section in Fig. 10

limit strain  $\epsilon_{cu} = 0.0035$ . Points of the ultimate limit state surface are plotted as blue squares while the yield surface is represented by red circles. The black arrows link points  $\mathbf{t}_y[\epsilon_k]$  and  $\mathbf{t}_\epsilon[\epsilon_k, \epsilon_{cu}]$  corresponding to the same strain mechanism  $\epsilon_k$ .

In general, the points belonging to both the rectangular and the L-shaped cross section present a drift towards smaller values of the axial force while the error concerning the bending moments looks to be correlated to the one affecting the axial force.

It is worth being emphasized that, for  $\epsilon_{cu} = 0.0035$  and regardless of the proximity between the yield and the ULS surface, all the computed strain mechanisms show non negligible drifts. In this sense, fixed a point  $\mathbf{t}_\epsilon[\epsilon_k, \epsilon_{cu}]$  of the ULS surface, the closest point belonging to the yield surface does not necessarily correspond to the same strain mechanism.

Such a difference becomes sensibly smaller for greater values of  $\epsilon_{cu}$ , as shown in Fig. 14 which refers to  $\epsilon_{cu} = 0.0085$ .

It is worth being emphasized that the use in seismic analysis of a ultimate strain value of  $\epsilon_{cu} = 0.0035$  is in contrast with the philosophy of structural provisions, and in particular Eurocode 8, which define the seismic action by means of a structural value. This is introduced in order to take into account the post-yielding behavior of the structural members which occurs far after strains of  $\epsilon_{cu} = 0.0035$ .

A numerical estimate of the domain drift can be performed by evaluating the specific internal works

associated with each point of the yield and the ULS surfaces; they are given by, respectively

$$w_y[\epsilon_k] = \mathbf{t}_y[\epsilon_k] \cdot \epsilon_k \tag{18}$$

$$w_\epsilon[\epsilon_k, \epsilon_{cu}] = \mathbf{t}_\epsilon[\epsilon_k, \epsilon_{cu}] \cdot \epsilon_k \tag{19}$$

Analogously to Eq. (15) we define the relative error  $\mathcal{E}_\epsilon(\epsilon_k)$  as the ratio:

$$\mathcal{E}_\epsilon(\epsilon_k) = \frac{w_y[\epsilon_k] - w_\epsilon[\epsilon_k, \epsilon_{cu}]}{w_\epsilon[\epsilon_k, \epsilon_{cu}]} \tag{20}$$

and compute in accordance the maximum  $\mathcal{E}_{\epsilon, \max}$ , average  $\bar{\mathcal{E}}_\epsilon$  and mean-square  $\hat{\mathcal{E}}_\epsilon$  values as:

$$\mathcal{E}_{\epsilon, \max} = \max \left| \frac{w_y[\epsilon_k] - w_\epsilon[\epsilon_k, \epsilon_{cu}]}{w_\epsilon[\epsilon_k, \epsilon_{cu}]} \right| \tag{21}$$

$$\bar{\mathcal{E}}_\epsilon = \frac{1}{n} \sum_{k=1}^n \left[ \frac{w_y[\epsilon_k] - w_\epsilon[\epsilon_k, \epsilon_{cu}]}{w_\epsilon[\epsilon_k, \epsilon_{cu}]} \right] \tag{22}$$

$$\hat{\mathcal{E}}_\epsilon = \sqrt{\frac{1}{n} \sum_{k=1}^n \left[ \left( \frac{w_y[\epsilon_k] - w_\epsilon[\epsilon_k, \epsilon_{cu}]}{w_\epsilon[\epsilon_k, \epsilon_{cu}]} \right)^2 \right]} \tag{23}$$

where  $n$  represents the number of sampled points (Figs. 15, 16).

Values of  $\mathcal{E}_{\epsilon, \max}$ ,  $\bar{\mathcal{E}}_\epsilon$  and  $\hat{\mathcal{E}}_\epsilon$ , computed for the rectangular cross section in Fig. 4 and for the L-shaped cross section in Fig. 10, are reported in Tables 4 and 5, respectively.

As expected errors decrease, almost proportionally, with respect to the ultimate strain; moreover, for both

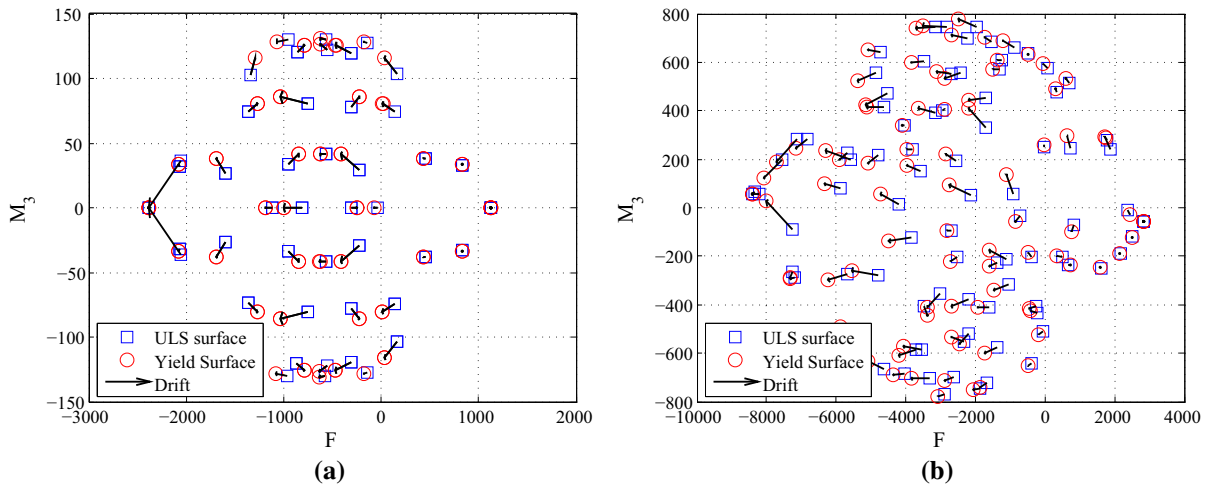


**Fig. 14** Projection of the domain drift for  $\epsilon_{cu} = 0.0085$ . **a** Rectangular section in Fig. 4 and **b** L-shaped section in Fig. 10

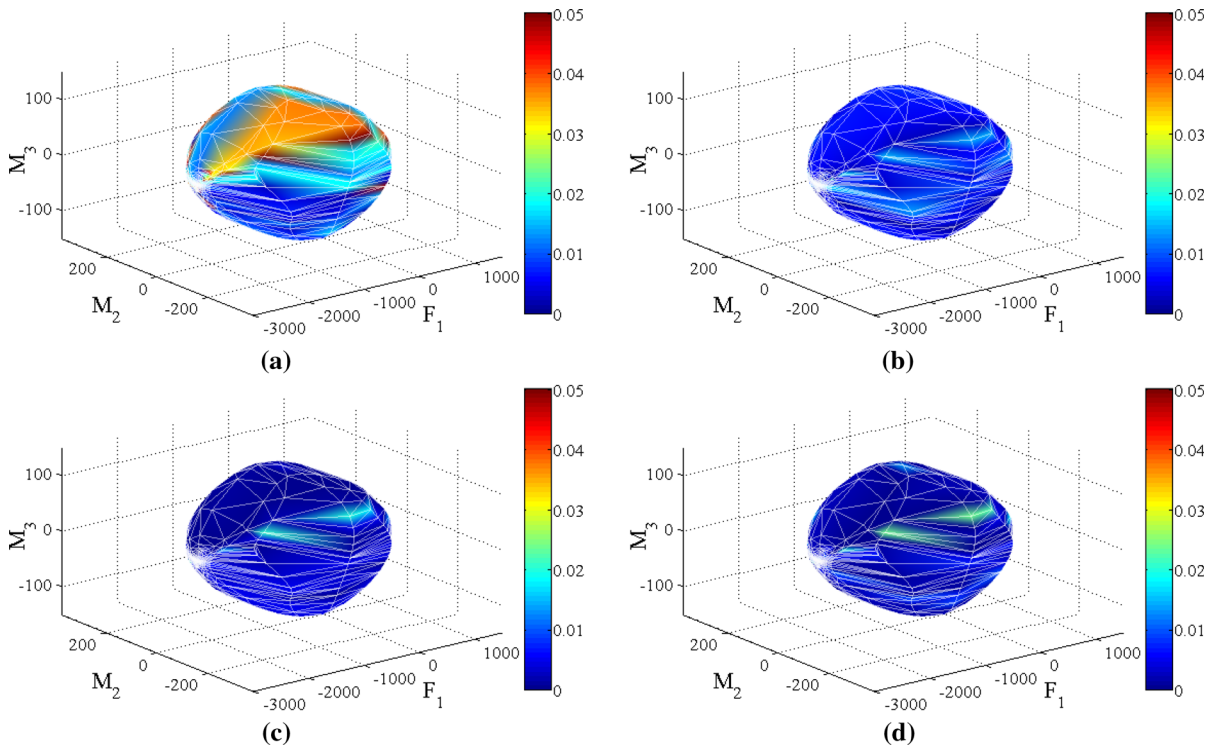


**Fig. 15** Rectangular section in Fig. 4. Contour plot of the differences between the yield surface and the ultimate limit state surfaces for increasing values of concrete ultimate strain. **a**  $\epsilon_{cu} = 0.0035$  · **b**  $\epsilon_{cu} = 0.0060$  · **c**  $\epsilon_{cu} = 0.0085$  · **d**  $\epsilon_{cu} = 0.0110$

the considered cross sections, error average turns out to be less than 5% already for  $\epsilon_{cu} = 0.006$ .

It can be observed that values of  $\hat{\mathcal{E}}_e$  turn out to be greater than the error averages, though having the same order of magnitude. This is not surprising since

mean square  $\hat{\mathcal{E}}_e$  is a more conservative measure of the distance between the two surfaces since it overcomes the possible presence of points with positive and negative errors.

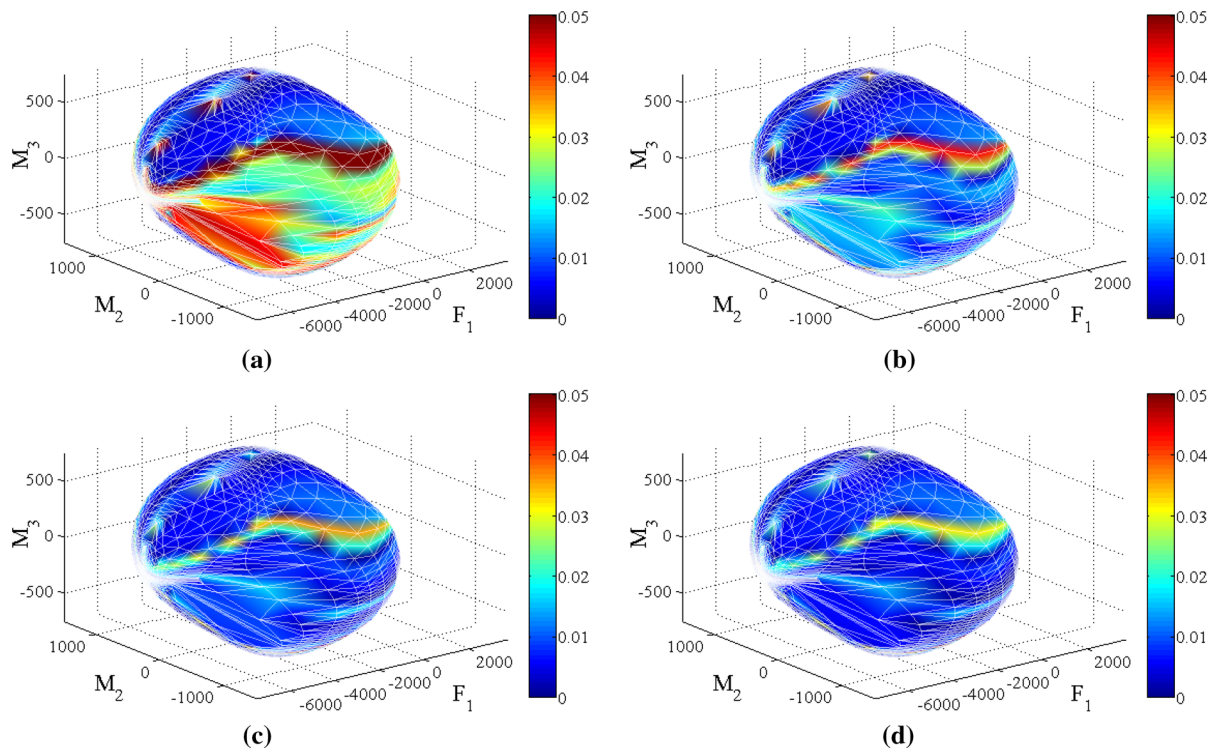


**Fig. 16** L-shaped section in Fig. 10. Contour plot of the differences between the yield surface and the ultimate limit state surfaces for increasing values of concrete ultimate strain. **a**  $\epsilon_{cu} = 0.0035$ . **b**  $\epsilon_{cu} = 0.0060$ . **c**  $\epsilon_{cu} = 0.0085$ . **d**  $\epsilon_{cu} = 0.0110$

**Table 4** Specific internal work relative error: rectangular section in Fig. 4

| $\epsilon_{cu}$ | Average $\bar{\mathcal{E}}_e$ (%) | Mean-square $\hat{\mathcal{E}}_e$ (%) | Maximum $\mathcal{E}_{e,max}$ (%) |
|-----------------|-----------------------------------|---------------------------------------|-----------------------------------|
| 0.0035          | 8.99                              | 10.82                                 | 19.05                             |
| 0.0060          | 2.95                              | 3.51                                  | 6.81                              |
| 0.0085          | 1.49                              | 1.84                                  | 2.94                              |
| 0.0110          | 0.86                              | 1.12                                  | 2.13                              |

**Table 5** Specific internal work relative error: L-shaped section in Fig. 10

| $\epsilon_{cu}$ | Average $\bar{\mathcal{E}}_e$ (%) | Mean-square $\hat{\mathcal{E}}_e$ (%) | Maximum $\mathcal{E}_{e,max}$ (%) |
|-----------------|-----------------------------------|---------------------------------------|-----------------------------------|
| 0.0035          | 10.22                             | 11.85                                 | 21.71                             |
| 0.0060          | 3.53                              | 4.16                                  | 8.11                              |
| 0.0085          | 1.78                              | 2.13                                  | 4.53                              |
| 0.0110          | 1.03                              | 1.24                                  | 2.68                              |

Recalling that ultimate strain value  $\epsilon_{cu} = 0.0085$  can be reasonably adopted for the considered sections because of the stirrup configuration (see, e.g. Fig. 5), the relative error average turns out to be less than 2% while the maximum error results less than 5% for both sections.

In conclusion, the results presented in this subsection point out how the error between the generalized forces computed by the yield and the ULS surfaces for a given strain mechanism is sufficiently low to justify the use of the yield surface for nonlinear frame analysis.

### 5 Conclusions

It has been presented a comparison between the capacity domains of two reinforced concrete cross sections obtained by the classical ultimate limit state procedure and by a limit analysis performed under the hypothesis of infinite ductility.

In particular, the yield surface, i.e. the capacity surface obtained via limit analysis, has been computed

by neglecting the contribution of the unconfined concrete cover. Such an assumption has been justified by an investigation concerning the bending moment–curvature curves of a rectangular cross section in case of uniaxial and biaxial bending, showing that the concrete cover has a very limited influence of the ULS generalized stress. Moreover, the usual assumptions underlying the conventional strength safety checks provided by Eurocodes [9], aiming at ensuring sufficient ductility to the concrete core, unavoidably results in the cover collapse.

A numerical comparison between the yield and the ULS surfaces proves that, in case of confinement ratios usually enforced by codes, the ductility is sufficient enough to make the yield surface approximate the ULS surface with a maximum error of about 5%. Moreover, considering that the error averages result less than 1%, the yield surface can reasonably approximate the ULS surface in procedures aiming to perform force-based safety checks of reinforced concrete cross sections.

Moreover, a comparison based on consistent strain mechanisms shows that the relative error of the virtual work, computed at all points of the yield and ULS surfaces for the corresponding strain mechanisms, turns out to be limited. This result is encouraging for using the yield surface to surrogate the response of the cross section for a given value of the generalized strain, in performing path-following analyses, and, more in general, in performing plastic analyses although further investigations are required.

However, this possible extensions does not impair the chance of a wider use of elastic domains in common practice. In particular, safety checks usually introduced in standard codes are based on internal forces obtained via spectral analyses. To this end, results presented in Sect. 4.1 present errors which are far less than approximations introduced by limited knowledge of the real structures as well as by randomness and uncertainties of both constitutive laws and external actions.

In the authors' opinion, simplified or conventional analysis approaches, capable of evaluating structural safety factors in a reliable way and providing essential information strictly related to the design process, are far more convenient in common practice than excessively detailed procedures. In fact, a complex modeling process is often in contrast with the lack of knowledge of the physical phenomenon and can

uselessly compromise a thorough control of designers on the analysis process.

Future research will focus on the characterization of a surrogate model, based on limit analysis, capable of reproducing the nonlinear response of reinforced concrete cross sections for a given value of the generalized strain. Such a tool would permit fast path-following analyses of complex structures, particularly appealing for computationally demanding applications. In particular, the convenient representation of the yield surface by Minkowski sum can be efficiently employed in sensitivity algorithms required by reliability [15, 28] and nonlinear random vibration analysis of structures [8]. Moreover, yield surface features can be profitably used in implementing mixed beam models capable of modelling non-uniform warping and buckling.

Finally, a further research outline will concern safety checks [19, 29] of recently developed shell elements [11, 38] in order to provide reliable and affordable tools oriented to common practice applications.

#### Compliance with ethical standards

**Conflict of interest** The authors declare that they have no conflict of interest.

#### References

1. Bilotta A, Garcea G, Leonetti L (2016) A composite mixed finite element model for the elasto-plastic analysis of 3D structural problems. *Finite Elem Anal Des* 113(Suppl C):43–53
2. Bing L, Park R, Tanaka H (2000) Constitutive behavior of high-strength concrete under dynamic loads. *ACI Struct J* 97(4):619–629
3. Bleyer J, De Buhan P (2013) Yield surface approximation for lower and upper bound yield design of 3d composite frame structures. *Comput Struct* 129:86–98
4. Casciaro R, Garcea G (2002) An iterative method for shakedown analysis. *Comput Methods Appl Mech Eng* 191(49–50):5761–5792
5. Chandler A, Lam N (2001) Performance based design in earthquake engineering a multidisciplinary review. *Eng Struct* 23:1525–1543
6. Chiorean C (2010) Computerised interaction diagrams and moment capacity contours for composite steel concrete cross-sections. *Eng Struct* 32(11):3734–3757
7. Chiorean C (2013) A computer method for nonlinear inelastic analysis of 3d composite steelconcrete frame structures. *Eng Struct* 57(Suppl C):125–152

8. Ditlevsen OD, Madsen HO (1996) Structural reliability methods. Wiley, Chichester
9. European Union: EN 1992—Eurocode 2: Design of concrete structures (1992)
10. European Union: EN 1998-1-3—Eurocode 8: Design of structures for earthquake resistance (1998)
11. Ile N, Frau A (2017) Use of response envelopes for seismic margin assessment of reinforced concrete walls and slabs. *Nucl Eng Des* 314(Suppl C):238–250
12. Karsan ID, Jirsa JO (1969) Behavior of concrete under compressive loading. *J Struct Div* 95(12):2543–2563
13. Karthik M, Mander J (2011) Stress-block parameters for unconfined and confined concrete based on a unified stress–strain model. *J Struct Eng* 137(2):270–273
14. Kent DC, Park R (1971) Flexural members with confined concrete. *J Struct Div* 97(7):1969–1990
15. Kim JH, Lee HS (2017) Reliability assessment of reinforced concrete rectangular columns subjected to biaxial bending using the load contour method. *Eng Struct* 150(Suppl C):636–645
16. Koiter WT (1960) General theorems for elasticplastic solids. In: Sneddon IN, Hill R (eds) *Progress in solid mechanics*. North-Holland, Amsterdam
17. Leonetti L, Le CV (2016) Plastic collapse analysis of Mindlin–Reissner plates using a composite mixed finite element. *Int J Numer Methods Eng* 105(12):915–935
18. Leonetti L, Casciaro R, Garcea G (2015) Effective treatment of complex statical and dynamical load combinations within shakedown analysis of 3D frames. *Comput Struct* 158:124–139
19. Loureno PB, Figueiras JA (1995) Solution for the design of reinforced concrete plates and shells. *J Struct Eng* 121(5):815–823
20. Lubliner J (2008) *Plasticity theory*. Dover, London
21. Malena M, Casciaro R (2008) Finite element shakedown analysis of reinforced concrete 3d frames. *Comput Struct* 86(11–12):1176–1188
22. Mander J, Priestley M, Park R (1988) Observed stress–strain behavior of confined concrete. *J Struct Eng* 114(8):1827–1849
23. Mander J, Priestley M, Park R (1988) Theoretical stress–strain model for confined concrete. *J Struct Eng* 114(8):1804–1826
24. Marmo F, Rosati L (2012) Analytical integration of elastoplastic uniaxial constitutive laws over arbitrary sections. *Int J Numer Methods Eng* 91:990–1022
25. Marmo F, Rosati L (2013) The fiber-free approach in the evaluation of the tangent stiffness matrix for elastoplastic uniaxial constitutive laws. *Int J Numer Methods Eng* 94:868–894
26. Marmo F, Rosati L (2015) Automatic cross-section classification and collapse load evaluation for steel/aluminum thin-walled sections of arbitrary shape. *Eng Struct* 100:57–65
27. Melan E (1938) Zur plastizität des räumlichen continuum. *Ing Arch* 9:116–126
28. Melchers RE (2002) *Structural reliability, analysis and prediction*, 2nd edn. Wiley, Chichester
29. Menun C (2003) A response-spectrum-based envelope for Mohr’s circle. *Earthq Eng Struct Dyn* 32(12):1917–1935
30. Menun C, Der Kiureghian A (2000) Envelopes for seismic response vectors—I: theory. *J Struct Eng* 126(4):467–473
31. Menun C, Der Kiureghian A (2000) Envelopes for seismic response vectors—II: application. *J Struct Eng* 126(4):474–481
32. Pastor F, Loute E (2005) Solving limit analysis problems: an interior-point method. *Commun Numer Methods Eng* 21(11):631–642
33. Priestley M, Seible F, Calvi GM (1996) *Seismic design and retrofit of bridges*. Wiley, New York
34. Scott BD, Park R, Priestley MJN (1982) Stress–strain behavior of concrete confined by overlapping hoops at low and high strain rates. *J Am Concrete Inst* 79(1):13–27
35. Sessa S, Marmo F, Rosati L (2015) Effective use of seismic response envelopes for reinforced concrete structures. *Earthq Eng Struct Dyn* 44(14):2401–2423
36. Simon JW (2012) Shakedown analysis with multidimensional loading spaces. *Comput Mech* 49:291–334
37. Spiliopoulos KV, Panagiotou KD (2017) An enhanced numerical procedure for the shakedown analysis in multidimensional loading domains. *Comput Struct* 193:155–171
38. Valoroso N, Marmo F, Sessa S (2014) Limit state analysis of reinforced shear walls. *Eng Struct* 61:127–139
39. Yan Y, Chirikjian GS (2015) Closed-form characterization of the Minkowski sum and difference of two ellipsoids. *Geom Dedicata* 177(1):103–128
40. Zouain N (2004) *Encyclopedia of computational mechanics*, chap. Shakedown and safety assessment. Wiley, Chichester, pp 291–334